nature materials

ARTICLES

https://doi.org/10.1038/s41563-022-01276-4

Check for updates

Halide perovskites enable polaritonic *XY* spin Hamiltonian at room temperature

Renjie Tao[1,7], Kai Peng[2,7], Louis Haeberlé[3], Quanwei Li[4], Dafei Jin[5], Graham R. Fleming[4], Stéphane Kéna-Cohen[3], Xiang Zhang[1,6] ✉ and Wei Bao[2] ✉

Exciton polaritons, the part-light and part-matter quasiparticles in semiconductor optical cavities, are promising for exploring Bose–Einstein condensation, non-equilibrium many-body physics and analogue simulation at elevated temperatures. However, a room-temperature polaritonic platform on par with the GaAs quantum wells grown by molecular beam epitaxy at low temperatures remains elusive. The operation of such a platform calls for long-lifetime, strongly interacting excitons in a stringent material system with large yet nanoscale-thin geometry and homogeneous properties. Here, we address this challenge by adopting a method based on the solution synthesis of excitonic halide perovskites grown under nanoconfinement. Such nanoconfinement growth facilitates the synthesis of smooth and homogeneous single-crystalline large crystals enabling the demonstration of *XY* Hamiltonian lattices with sizes up to 10 × 10. With this demonstration, we further establish perovskites as a promising platform for room temperature polaritonic physics and pave the way for the realization of robust mode-disorder-free polaritonic devices at room temperature.

Bose–Einstein condensation (BEC), first proposed in 1924, describes a quantum-statistical phase transition where, below the transition temperature, a substantial fraction of diluted bosonic particles spontaneously occupy the ground state and exhibit macroscopic quantum behaviours. The experimental realization of BEC condensates and their optical lattices in ultracold (approximately microkelvin) atoms enabled the field of analogue simulation, where complex many-body physics problems such as the formation of frustrated spin, superconductivity and superfluidity, to be experimentally tackled in a controllable manner[1–3]. Because of the complexity and extremely low temperature involved in using ultracold atoms, there have been great efforts recently towards building a room-temperature analogue simulator with solid-state BEC systems for practical applications[4–6].

In this context, semiconductor microcavities are an attractive platform. In a semiconductor optical cavity, exciton polaritons, hybrid light–matter quasiparticles, are formed when the coupling rate between excitons and photons is much faster than their respective dissipation rates. These bosonic polaritons have an ultra-small effective mass (~10^{-5} electron mass) inherited from the photon, as well as nonlinear interactions inherited from the exciton Coulombic interactions. Thus, polaritons can undergo BEC at much-elevated temperatures[4,6], ultimately limited by the exciton binding energy. Polariton condensation was first realized in quantum-well microcavities grown with molecular beam epitaxy (MBE)[7,8], where liquid helium temperatures (~4 K) must be maintained to prevent exciton autoionization. Although high exciton binding energy materials, such as organic molecules, show potential for room-temperature polaritonics[9–12], they unfortunately have severe limitations on sample size, homogeneity, polariton lifetime and/or nonlinear interaction strength. Therefore, the large and homogeneous MBE-grown GaAs quantum well remains the only exciton–polariton platform (though at low temperature) where interesting physics, such as soliton formation[13,14], *XY* spin Hamiltonian[15] and topological effects[16,17], have been experimentally explored. This is primarily attributed to two reasons: the maturity of high-quality MBE material growth and patterning, and the strongly interacting excitons of the GaAs quantum wells at liquid helium temperature.

Recently, semiconducting lead halide perovskites have emerged as contenders to GaAs for polaritonics but at room temperature due to their large exciton binding energy[18–20], high photoluminescence (PL) quantum yield[21], tunable bandgap[22] and high room-temperature nonlinear interaction strength[23]. With chemical vapour deposition (CVD), single-crystalline inorganic halide perovskites have shown polariton condensation[24,25]. However, due to the limitations of the current growth methods and the fragile nature of perovskites, only small single crystals can be integrated into the optical cavity (Supplementary Fig. 1). Critically, the small sizes prohibit the studies of the aforementioned large-scale phenomena due to the limited lattice size and the restricted propagation lengths[26].

In this work, we overcome these limitations by direct solution growth of various types of large-area halide perovskite single crystals inside optical nanocavities. Due to the uniform confined environment, our solution growth approach shows uniformity, comparable to the MBE-grown GaAs quantum well, enabling submillimetre-size large single crystals with superb excitonic quality. These crystals with strongly interacting Wannier–Mott excitons allowed us to successfully demonstrate a polaritonic *XY* spin Hamiltonian with all-inorganic perovskite $CsPbBr_3$ at room temperature. Further, we show that a lattice with a large number of coherently coupled condensates up to 10 × 10 can be achieved. This is an important step towards the ultimate goal of realizing a room-temperature polaritonic platform on par with MBE-grown GaAs at low temperatures. In addition, we show that the dispersion of the perovskite system has unique advantages for future studies on synthetic non-Abelian gauge fields and topological physics. Our work establishes a robust

[1]Nanoscale Science and Engineering Center, University of California, Berkeley, CA, USA. [2]Department of Electrical and Computer Engineering, University of Nebraska-Lincoln, Lincoln, NE, USA. [3]Department of Engineering Physics, École Polytechnique de Montréal, Montréal, Quebec, Canada. [4]Department of Chemistry, University of California, Berkeley, CA, USA. [5]Center for Nanoscale Materials, Argonne National Laboratory, Lemont, IL, USA. [6]Faculty of Science and Faculty of Engineering, The University of Hong Kong, Hong Kong, China. [7]These authors contributed equally: Renjie Tao, Kai Peng
✉e-mail: xiang@berkeley.edu; wbao@unl.edu

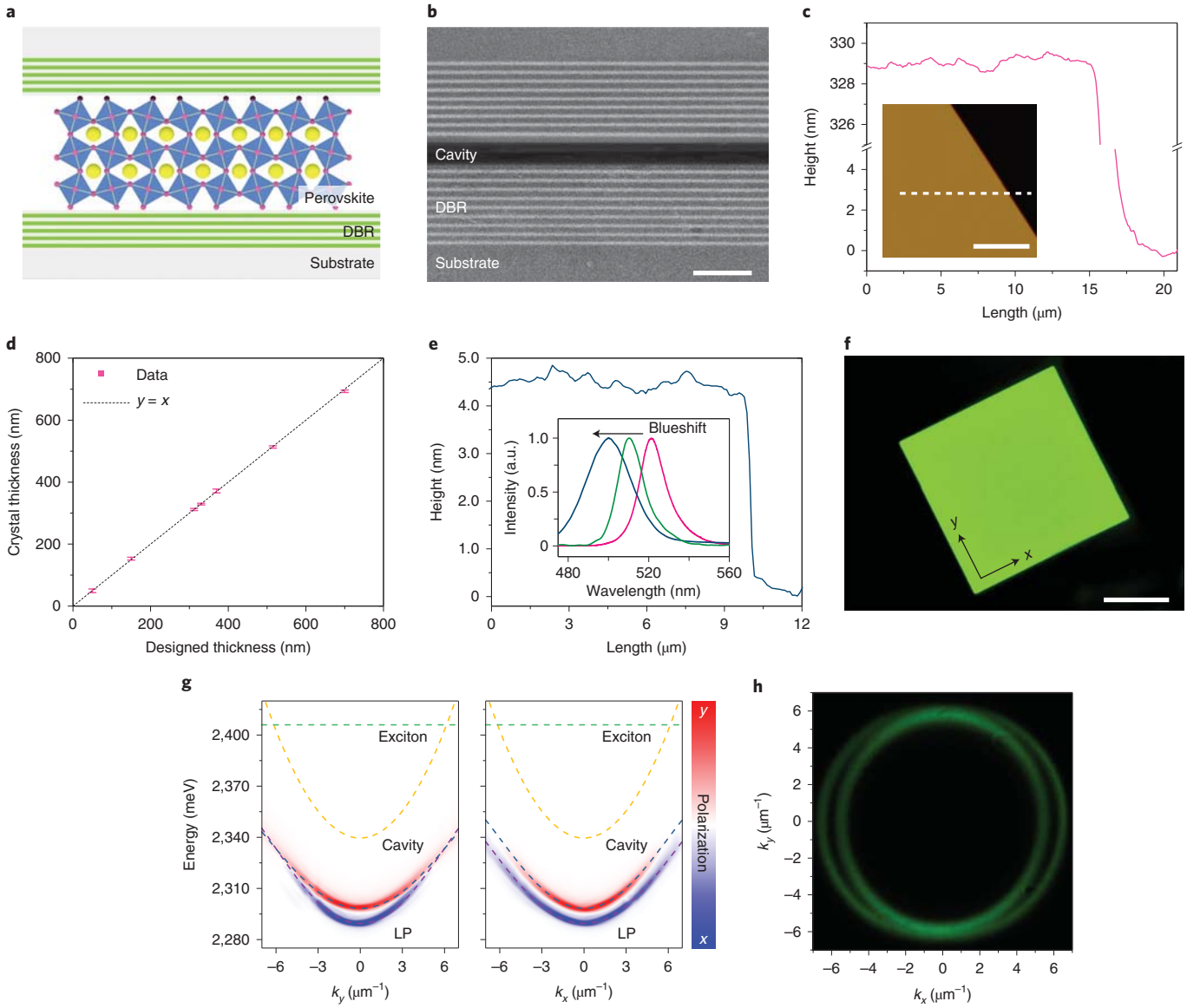

Fig. 1 | Synthesis and characterization of single-crystalline excitonic halide perovskites in DBR nanocavities. a, By using deposited pillar arrays (Supplementary Fig. 2) as spacers and bonders in between two DBR mirrors (nine pairs of SiO_2 and Ta_2O_5 alternating layers), a nanocavity of a designed height for halide perovskite crystals is formed so that the detuning between exciton and photon can be controlled. **b**, The scanning electron microscopy cross-sectional image of a fabricated nanocavity. Scale bar, 1 μm. **c**, The after-growth cavities are opened. The crystal thickness controllability and uniformity is revealed by AFM imaging (inset) and a cross-section profile (the white dashed line in the insert); the thickness of as-synthesized crystal from the nanocavity is ~329 nm (±0.4 nm), which matches the designed height of the nanocavity (~330 nm). Scale bar, 10 μm. **d**, This nanometre-scale-precision thickness can be well controlled in a wide range as measured by AFM. The <1.6% of thickness variance across each chip (2 cm size) is caused by pillar film deposition uniformity. **e**, When shrinking the nanocavity height to only a few nanometres, the $CsPbBr_3$ crystals show a thickness of only 4.45 ± 0.35 nm and strong quantum-confinement-induced blueshifted PL (inset blue curve) down to 499 nm. The green curve in the inset corresponds to a measured thickness of 7.3 ± 0.5 nm (Supplementary Fig. 9b). **f**, A typical $CsPbBr_3$ crystal grown in the nanocavity shows uniform and bright PL across hundreds of micrometres. Scale bar, 100 μm. **g**, The linear-polarized PL of polariton dispersions (energy vs. wavevector *k*) along the *y* and *x* axes (two crystal axes as shown in **f**). The dashed lines are the fittings of the two lower branches (LP; red and blue), exciton energy (green) and cavity (orange) modes.. The two lower polariton branches with polarization along *x* (blue) and *y* (red) axis cross at the diabolic points at $k_y = 5.9\ \mu m^{-1}$. **h**, The cross-section of the two polariton branches (PL measurement) in k-space at diabolic points with the energy of 2,332.5 meV, illustrating the Rashba-like spin–orbital coupling.

and excellent platform for room-temperature polaritonics and also paves the way for many other nonlinear polaritonic devices for practical applications.

Device synthesis and characterization

The key that enables our synthesis of high-quality perovskite crystals for large-scale polaritonics and the subsequent realization of the polaritonic *XY* spin Hamiltonian at room temperature is the solution synthesis of halide perovskites directly within prefabricated optical nanocavities (a combination of top-down fabrication and bottom-up synthesis; schematic depiction in Supplementary Fig. 2), inspired by previous efforts in organic polariton growth[27] and recent halide perovskite growth[28]. We first deposited high-quality distributed Bragg reflector (DBR) multilayers on the quartz

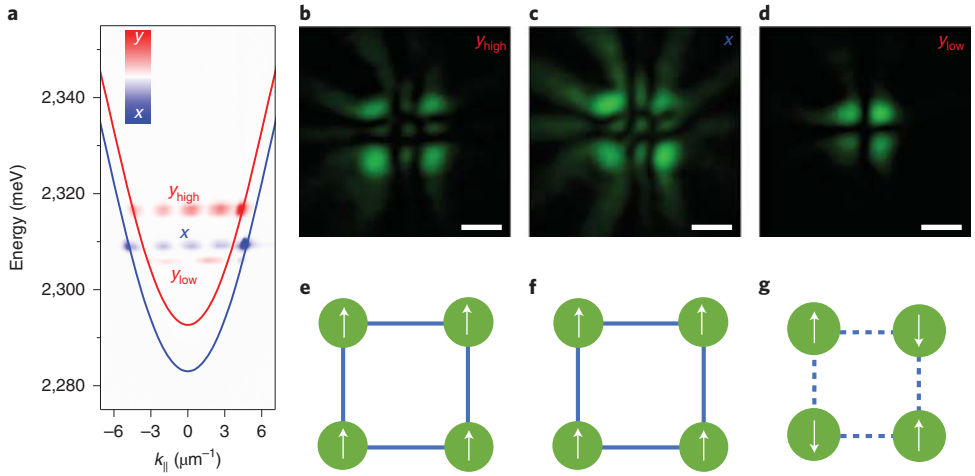

Fig. 2 | Room-temperature demonstration of polariton *XY* Hamiltonian square 2 × 2 lattices. a–d, Time-integrated k-space polariton dispersion before (the solid lines) and after (lines of dots) the condensation (**a**). The polariton condenses simultaneously at two lower branches with perpendicular polarization. At the branch with *x* polarization, the condensation occurs at $k_c = 4.95\,\mu m^{-1}$. The odd number of interference fringes in the corresponding real-space image (**c**) shows an in-phase coupling. At the branch with *y* polarization, the condensation occurs at two different wave vectors (y_{high}, $k_c = 4.3\,\mu m^{-1}$; y_{low}, $k_c = 3.2\,\mu m^{-1}$). Panels **b** and **d** are the time-integrated real-space images of y_{high} and y_{low}, respectively. The intrinsic oscillatory lattice dynamics mechanism reduces the oscillation between the two condensation states with opposite phases and different coupling: in-phase for y_{high} and antiphase for y_{low}. **e–g**, Diagrams of spin configurations of condensations y_{high}, *x* and y_{low}, corresponding to the real-space images of **b**, **c** and **d**, respectively. Panels **e** and **f** show the antiferromagnetic coupling (solid blue lines) with parallel spins, and **g** shows ferromagnetic coupling (dashed blue lines) with antiparallel spins between neighbouring sites. Scale bars in **b**, **c** and **d**, 2 μm.

substrates. Two of these DBR substrates were then bonded together via a thermal compression bonding process with prepatterned gold pillars as the spacers (Methods and Supplementary Fig. 3), creating a symmetric two-dimensional (2D) confined nanocavity (Fig. 1b) to serve as the optical cavity as well as the crystal growth environment. Chemical reaction and crystal growth under nanometre confinement are different than in traditional methods (Methods and Supplementary Fig. 1), and the resulting single-crystalline perovskite crystals are very large (>300 μm; Supplementary Fig. 4) due to a substantially decreased nucleation rate (Supplementary Fig. 6)[29]. In addition, the nanoconfined environment also leads to evaporation only from the nanocavities' exposed edges, resulting in a slow crystal growth rate[30] and thus excellent crystallinity, as evidenced by the sharp X-ray diffraction peaks (Supplementary Fig. 5). To demonstrate its broad applicability, we synthesized three emerging excitonic halide perovskites (Supplementary Fig. 4)—the all-inorganic bromide perovskite $CsPbBr_3$, the 2D iodide layered perovskite $(C_6H_5C_2H_4NH_3)_2PbI_4$ (phenylethylamine lead iodide, PEPI) and the organic–inorganic hybrid chloride perovskite $MAPbCl_3$—all with submillimetre crystal sizes and high crystallinity (Supplementary Fig. 5). Compared with previously reported layer-by-layer stacking of polaritonic devices, our approach produced a laterally large size, yet vertically controllable, nanoscale-thin, single-crystalline halide perovskites free from damage or the contamination from traditional fabrication due to the use of prebonded ultra-flat DBR mirrors (Supplementary Figs. 7 and 8). At the same time, this fabrication design also produces pristine DBR optical reflectivity, which indicates excellent potential for future studies of near thermal equilibrium polariton BEC.

Our work combines large lateral size, nanometre-precision thickness control, homogeneity and excellent excitonic properties as required for large-scale room-temperature polaritonics. The precise control over the crystal thickness here enables accurate tuning of the photonic mode and hence the emission dynamics of the polariton mode. To demonstrate the excellent crystal thickness control and uniformity, we performed atomic force microscopy (AFM) of our $CsPbBr_3$ crystal. The height profile (Fig. 1c) reveals a 329 ± 0.4 nm range (~0.12% variance) across a lateral distance of 20 μm (Fig. 1c inset). This measured height matches well with the designed cavity height (~330 nm; Fig. 1b). By designing cavities of various heights (adjusting the pillar height between DBR substrates), we observed that the crystal grew to fill the cavities completely, with minimal deviation (Fig. 1d). The fully filled cavities in the perovskite chemical synthesis lead to excellent thickness homogeneity, which results in small polariton mode disorders (Supplementary Fig. 14); these cavities are distinct from the partially filled cavities in organics' physical recrystallization, which have substantial polariton mode inhomogeneity[27]. Across 50 to 700 nm, the crystal thickness control shows nanometre-scale precision, with less than 1.6% of the variance across each chip (2 cm size) caused by pillar film deposition uniformity. In addition, we also achieved a cavity thickness down to 4.45 ± 0.35 nm (Fig. 1e and Supplementary Fig. 9), limiting the crystal thickness to a few unit cells. This quantum confinement even led to control over the excitonic energy level.

This method also allows us to fully take advantage of the perovskites' excellent optical properties. PL mapping under ultraviolet excitation showed excellent optical homogeneity (Fig. 1f and Supplementary Figs. 10 and 14); a long PL lifetime (Supplementary Fig. 11), pointing to low non-radiative loss; and a narrow PL emission peak (Supplementary Fig. 12). More importantly, robust excitons were observed at room temperature, supported by the strong excitonic absorption peak (Supplementary Fig. 13). The optical properties, combined with the high reflectivity of the DBR mirrors (cavity quality factor $Q \approx 900$ with two symmetric nine pairs DBR mirrors on both sides of the perovskites), resulted in the strongly coupled exciton polaritons (Fig. 1g). Due to the high optical quality and precise detuning control of the solution-grown $CsPbBr_3$ perovskite sample, a room-temperature polariton BEC at $k_{||} = 0$ ($k_{||}$ is the in-xy-plane wavevector) with non-resonant excitation was readily observed (Supplementary Figs. 16 and 17).

More interestingly, due to the orthorhombic crystal structure of $CsPbBr_3$ at room temperature, optical birefringence breaks

the degeneracy of the two photonics transverse-electric and transverse-magnetic modes at $k_{\parallel}=0$ (ref. [25]; Fig. 1g). The combination of noticeable optical birefringence and spin–orbit coupling that arises from transverse-electric/transverse-magnetic mode splitting in $CsPbBr_3$ creates an interesting k-space dispersion[31] (Fig. 1g) along with the x and y directions (two crystal axes as shown in Fig. 1f). This dispersion effectively creates a synthetic gauge field on the flowing polariton condensate and is predicted to be Rashba-like around the two diabolical points (Fig. 1g,h)[31], where the two polariton branches exactly cross. In contrast to the organics[32–34], the nonlinearity and homogeneity in our perovskites are much superior. Thus, the perovskite microcavities also provide a unique room-temperature playground for future large-scale and nonlinear studies on non-Abelian gauge fields[17,31,35] and topological physics[36].

Construction of *XY* spin Hamiltonian

Given the large and homogeneous samples with interesting polariton dispersion, we were able to explore the potential and limits of our approach by performing the room-temperature polariton graphs of the *XY* Hamiltonian minimizer demonstration with $CsPbBr_3$ perovskites. Many complex optimization problems can be mapped into microscopic spin models with rich macroscopic behaviours such as a distinct Kosterlitz–Thouless[37] phase transition. However, compared with other lithographically patterned polariton lattices[38,39], experimentally implementing *XY* Hamiltonian lattices at room temperature is one of the most challenging tasks due to the stringent sample requirements. Thus, a successful construction has only been reported at 10 K with the best MBE-grown GaAs quantum-well microcavities[15,40], where both excellent sample homogeneity (within a few millielectronvolts potential disorders/variations) and large sample size requirements can be met simultaneously.

Here, taking advantage of nanoconfinement-grown perovskites, we finally construct the polaritonic *XY* spin Hamiltonian at room temperature by non-resonantly exciting polariton lattice patterns with a reflective spatial light modulator (schematics in Supplementary Fig. 15). PL images of the condensate lattice were collected in a transmission configuration to control the excitation and the signal collection separately. Because of the strong polariton–polariton repulsive interaction originating from the Coulombic interaction among excitons, the polaritons under condensation will have a non-zero in-plane momentum and expand ballistically[41,42] with a small excitation laser spot (Supplementary Fig. 18). When these expanding condensates are brought closer, interference and coupling occur, leading to phase synchronization between the condensates[43]. According to the complex Ginzburg–Landau equation model in previous analysis[15], the total amount of polaritons N_{XY} can be approximated as $N_{XY}=N_{iso}+\sum_{ij}J_{ij}\cos\left(\theta_i-\theta_j\right)$, where N_{iso} is the total polariton number with full isolated sites (infinite distance), $\theta_i-\theta_j$ is the phase difference between two condensates and J_{ij} is the nearest neighbour coupling strength. The final macroscopic coherent state will have the highest possible polaritonic occupancy to minimize the polariton losses[44]. Thus, in the ideal cases, the relative phase difference between condensates can be used as pseudo-spins and provides a route to search the global minimum in the *XY* Hamiltonian[15,40,44], $H_{XY}=-\sum_{ij}J_{ij}\cos\left(\theta_i-\theta_j\right)$. When the Josephson coupling is negligible, the coupling strength J_{ij} has an oscillating characteristic as a function of $k_c d$, where k_c is the outflow in-plane momentum and d is the distance between the two adjacent condensates.[15,41] This results in ferromagnetic (positive sign) and antiferromagnetic (negative sign) couplings between sites, as demonstrated in Supplementary Figs. 22 and 23 for a polariton dyad configuration. Thus, by changing the geometry of the polariton lattice via a spatial light modulator, different *XY* spin Hamiltonians can be readily constructed.

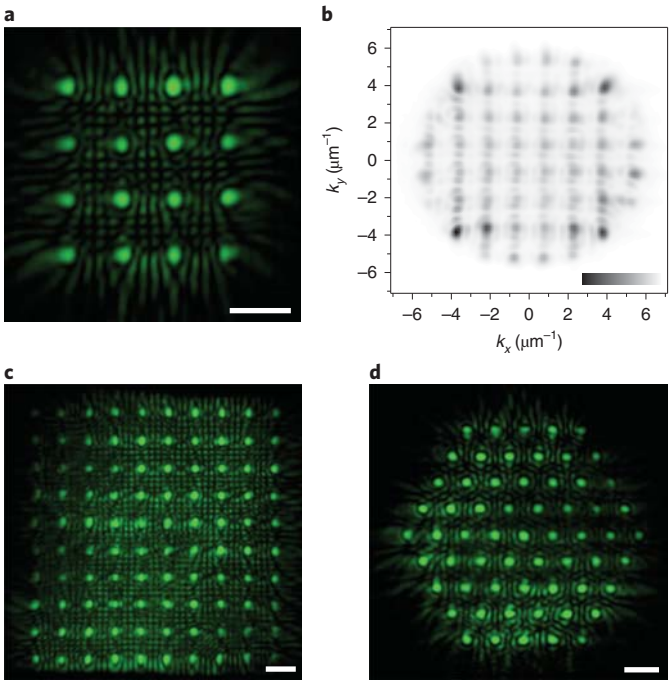

Fig. 3 | Extended polariton lattices. a,**b**, Time-integrated real-space and k-space images of a 4×4 polariton lattice with antiferromagnetic coupling. The even interference fringes can be clearly identified. In the colour bar in **b**, black is high intensity and white is low intensity. **c**, Time-integrated real-space image of a 10×10 polariton lattice with antiferromagnetic coupling. **d**, Time-integrated real-space image of a triangular polariton lattice with ferromagnetic coupling. Scale bars in **a**, **c** and **d**, 5 μm.

When a 2×2 lattice was excited in $CsPbBr_3$ microcavities with a fixed laser spot distance of ~1.5 μm, in contrast with GaAs, the two split lower polariton branches with perpendicular polarizations (Supplementary Fig. 18) condense simultaneously at three slightly different k-space locations (Fig. 2a). The x-polarization branch condenses at $k_c=4.95\,\mu m^{-1}$ with an odd number of interference fringes in k-space dispersion images (line of blue dots in Fig. 2a). The corresponding four real-space condensates (Fig. 2c) also have the same phase, indicating a ferromagnetic coupling as in the spin diagram shown in Fig. 2f. For the y-polarization branch, both ferromagnetic and antiferromagnetic configurations were identified. While the condensates with higher $k_c=4.3\,\mu m^{-1}$ (y_{high}) are synchronized to have the same phase (Fig. 2b), the lower $k_c=3.2\,\mu m^{-1}$ condensates (y_{low}) have a π phase difference between the neighbours (Fig. 2d). The antiphase interference effect also induces the condensates to be closer, consistent with low-temperature GaAs cases[15]. This coexistence of both in-phase and antiphase synchronization of the same polarization branch is due to the intrinsic oscillatory lattice dynamics[45]. In addition, a 90° compass spin model can also be realized with an asymmetrical square configuration (Supplementary Fig. 25).

For the future study of phase transitions in interacting bosonic systems such as the Kosterlitz–Thouless transition with a polariton, it is essential to construct a large-scale, homogeneous and coherently coupled lattice. Towards this goal, we gradually increase the node number of the polariton lattices and tune the lattice geometry simply by dynamically changing the spatial light modulator excitation pattern. High-quality real-space and k-space images of a 4×4 polariton lattice (Fig. 3a,b) are first achieved. The even number of real-space interference fringes between the two neighbouring condensations (Fig. 3a) can be clearly seen, indicating an antiferromagnetic energy minimum state. In addition, the k-space image confirms the antiferromagnetic coupling with the characteristic

pattern, where the slightly lower-intensity centre spots are accompanied by higher-intensity Bragg diffraction peaks in the surrounding corner (Fig. 3b), similar to low-temperature GaAs cases[15]. Next, an 8×8 lattice is also easily constructed (Supplementary Fig. 26). In addition, the square lattice can be further extended to 10×10 coherently coupled condensates with a full lattice size of more than 50 μm. Again, an even number of interference fringes with excellent visibility in between neighbouring condensates suggest an antiferromagnetic coupling. The inhomogeneity of the condensates at the edge region is mainly caused by the polariton outflow (the particle outflow to the sites on the edge happens from fewer sites in comparison with the central sites), as shown in Fig. 3 and Supplementary Fig. 24, instead of the small disorders in our samples (lower polariton-mode spatial root-mean-square variations of only 1.02 meV in Supplementary Fig. 14). These intensity inhomogeneities play an essential role in changing the interactions and the phase difference distribution[44], which can be addressed in the future with feedback excitation schemes recently reported[40]. A real-space PL image of a sizable (40 μm) triangular lattice, one of the most important spin configurations in magnetism research[2,15], is also shown in Fig. 3d. In this case, the *XY* Hamiltonian is minimized when all polariton sites lock in phase and establish a ferromagnetic configuration.

Outlook

We emphasize that, to realize this room-temperature polaritonic *XY* Hamiltonian experiment, strongly interacting polaritons and large homogeneous samples are crucial to generate outflow condensates and to construct a large node lattice without being impacted by the crystal boundaries or disorders, respectively. Thanks to the Wannier–Mott excitons, the polariton–polariton interaction constant g (ref. [23]) in perovskite can be at least two orders of magnitude higher than in the organics with weakly interacting Frenkel excitons[46]. The stringent requirements of homogeneity (one almost needs disorder free), photo-stability and large sample size further hinder other room-temperature systems[10,11,24,25,47] from performing the above spin Hamiltonian experiments. In addition, the experimental room-temperature real-space polariton PL images from our solution-grown samples are comparable to the low-temperature MBE-grown GaAs case[15], which further justifies the high quality of our perovskite platform. The interesting dispersions of perovskite can lead to three sets of *XY* Hamiltonian patterns, due to condensation at three different k-space locations. Last but not least, future innovations on material platforms and optical technology are still highly sought to achieve practical *XY* spin Hamiltonian simulators for optimization problems, where one can precisely control the Hamiltonian at a more quantitative level with a substantially large lattice size.

To conclude, we solution-synthesized various types of halide perovskites using a nanoconfinement growth approach for room-temperature polaritonics. The resulting large-area but nanoscale-thickness crystals with excellent excitonic properties and homogeneity enabled us to demonstrate a polaritonic spin Hamiltonian lattice with a large size at room temperature. Our work establishes a robust room-temperature polaritonic platform for studying non-equilibrium physics. Given the pristine DBR optical reflectivity, the approach is also attractive for near thermal equilibrium polariton BEC at room temperature. The unique combination of intrinsically large optical birefringence and strongly nonlinear interacting polaritons is ideal for studies of quantum fluid physics in topological systems[31] and simulating a lithography-patterned[39] large 2D Hamiltonian with spin–orbital coupling[48]. The strong nonlinearity from Wannier–Mott excitons alone could also lead to many other device applications, such as a 2D topological polaritonic laser[16,49] and potential photonic simulator with synthetic gauge field[31,35], previously inaccessible at room temperature.

Online content

Any methods, additional references, Nature Research reporting summaries, source data, extended data, supplementary information, acknowledgements, peer review information; details of author contributions and competing interests; and statements of data and code availability are available at https://doi.org/10.1038/s41563-022-01276-4.

Received: 22 July 2021; Accepted: 4 May 2022;
Published online: 09 June 2022

References

1. Buluta, I. & Nori, F. Quantum simulators. *Science* **326**, 108–111 (2009).
2. Struck, J. et al. Quantum simulation of frustrated classical magnetism in triangular optical lattices. *Science* **333**, 996–999 (2011).
3. Gross, C. & Bloch, I. Quantum simulations with ultracold atoms in optical lattices. *Science* **357**, 995–1001 (2017).
4. Deng, H., Haug, H. & Yamamoto, Y. Exciton-polariton Bose-Einstein condensation. *Rev. Mod. Phys.* **82**, 1489–1537 (2010).
5. Boulier, T. et al. Microcavity polaritons for quantum simulation. *Adv. Quantum Technol.* **3**, 2000052 (2020).
6. Byrnes, T., Kim, N. Y. & Yamamoto, Y. Exciton–polariton condensates. *Nat. Phys.* **10**, 803–813 (2014).
7. Deng, H., Weihs, G., Santori, C., Bloch, J. & Yamamoto, Y. Condensation of semiconductor microcavity exciton polaritons. *Science* **298**, 199–202 (2002).
8. Kasprzak, J. et al. Bose–Einstein condensation of exciton polaritons. *Nature* **443**, 409–414 (2006).
9. Christopoulos, S. et al. Room-temperature polariton lasing in semiconductor microcavities. *Phys. Rev. Lett.* **98**, 126405 (2007).
10. Plumhof, J. D., Stoeferle, T., Mai, L., Scherf, U. & Mahrt, R. Room-temperature Bose–Einstein condensation of cavity exciton–polaritons in a polymer. *Nat. Mater.* **13**, 247–252 (2014).
11. Daskalakis, K. S., Maier, S. A., Murray, R. & Kéna-Cohen, S. Nonlinear interactions in an organic polariton condensate. *Nat. Mater.* **13**, 271–278 (2014).
12. Kang, J. W. et al. Room temperature polariton lasing in quantum heterostructure nanocavities. *Sci. Adv.* **5**, eaau9338 (2019).
13. Amo, A. et al. Polariton superfluids reveal quantum hydrodynamic solitons. *Science* **332**, 1167–1170 (2011).
14. Sich, M. et al. Observation of bright polariton solitons in a semiconductor microcavity. *Nat. Photon.* **6**, 50–55 (2012).
15. Berloff, N. G. et al. Realizing the classical *XY* Hamiltonian in polariton simulators. *Nat. Mater.* **16**, 1120–1126 (2017).
16. Klembt, S. et al. Exciton–polariton topological insulator. *Nature* **562**, 552–556 (2018).
17. Gianfrate, A. et al. Measurement of the quantum geometric tensor and of the anomalous Hall drift. *Nature* **578**, 381–385 (2020).
18. Zhang, Q. et al. High-quality whispering-gallery-mode lasing from cesium lead halide perovskite nanoplatelets. *Adv. Funct. Mater.* **26**, 6238–6245 (2016).
19. Passarelli, J. V. et al. Tunable exciton binding energy in 2D hybrid layered perovskites through donor–acceptor interactions within the organic layer. *Nat. Chem.* **12**, 672–682 (2020).
20. Baranowski, M. & Plochocka, P. Excitons in metal-halide perovskites. *Adv. Energy Mater.* **10**, 1903659 (2020).
21. Stranks, S. D. & Snaith, H. J. Metal-halide perovskites for photovoltaic and light-emitting devices. *Nat. Nanotechnol.* **10**, 391–402 (2015).
22. Sutherland, B. R. & Sargent, E. H. Perovskite photonic sources. *Nat. Photon.* **10**, 295–302 (2016).
23. Fieramosca, A. et al. Two-dimensional hybrid perovskites sustaining strong polariton interactions at room temperature. *Sci. Adv.* **5**, eaav9967 (2019).
24. Su, R. et al. Room-temperature polariton lasing in all-inorganic perovskite nanoplatelets. *Nano Lett.* **17**, 3982–3988 (2017).
25. Bao, W. et al. Observation of Rydberg exciton polaritons and their condensate in a perovskite cavity. *Proc. Natl Acad. Sci. USA* **116**, 20274–20279 (2019).
26. Su, R. et al. Perovskite semiconductors for room-temperature exciton-polaritonics. *Nat. Mater.* **20**, 1315–1324 (2021).
27. Kéna-Cohen, S., Davanço, M. & Forrest, S. R. Strong exciton-photon coupling in an organic single crystal microcavity. *Phys. Rev. Lett.* **101**, 116401 (2008).
28. Wang, X. D., Li, W. G., Liao, J. F. & Kuang, D. B. Recent advances in halide perovskite single-crystal thin films: fabrication methods and optoelectronic applications. *Sol. RRL* **3**, 1800294 (2019).
29. Chen, Z. et al. Thin single crystal perovskite solar cells to harvest below-bandgap light absorption. *Nat. Commun.* **8**, 1890 (2017).
30. Liu, Y. et al. Multi-inch single-crystalline perovskite membrane for high-detectivity flexible photosensors. *Nat. Commun.* **9**, 5302 (2018).

31. Terças, H., Flayac, H., Solnyshkov, D. D. & Malpuech, G. Non-Abelian gauge fields in photonic cavities and photonic superfluids. *Phys. Rev. Lett.* **112**, 066402 (2014).
32. Kéna-Cohen, S., Davanço, M. & Forrest, S. R. Resonant Rayleigh scattering from an anisotropic organic single-crystal microcavity. *Phys. Rev. B* **78**, 153102 (2008).
33. Rechcinska, K. et al. Engineering spin-orbit synthetic Hamiltonians in liquid-crystal optical cavities. *Science* **366**, 727–730 (2019).
34. Ren, J. et al. Nontrivial band geometry in an optically active system. *Nat. Commun.* **12**, 689 (2021).
35. Whittaker, C. E. et al. Optical analogue of Dresselhaus spin–orbit interaction in photonic graphene. *Nat. Photon.* **15**, 193–196 (2021).
36. Su, R., Ghosh, S., Liew, T. C. H. & Xiong, Q. Optical switching of topological phase in a perovskite polariton lattice. *Sci. Adv.* **7**, eabf8049 (2021).
37. kosterlitz, J. M. & Thouless, D. J. Ordering, metastability and phase transitions in two-dimensional systems. *J. Phys. C* **6**, 1181–1203 (1973).
38. Dusel, M. et al. Room temperature organic exciton–polariton condensate in a lattice. *Nat. Commun.* **11**, 2863 (2020).
39. Su, R. et al. Observation of exciton polariton condensation in a perovskite lattice at room temperature. *Nat. Phys.* **16**, 301–306 (2020).
40. Töpfer, J. D. et al. Engineering spatial coherence in lattices of polariton condensates. *Optica* **8**, 106–113 (2021).
41. Ohadi, H. et al. Nontrivial phase coupling in polariton multiplets. *Phys. Rev. X* **6**, 031032 (2016).
42. Wouters, M., Carusotto, I. & Ciuti, C. Spatial and spectral shape of inhomogeneous nonequilibrium exciton-polariton condensates. *Phys. Rev. B* **77**, 115340 (2008).
43. Tosi, G. et al. Geometrically locked vortex lattices in semiconductor quantum fluids. *Nat. Commun.* **3**, 1243 (2012).
44. Kalinin, K. P. & Berloff, N. G. Networks of non-equilibrium condensates for global optimization. *New J. Phys.* **20**, 113023 (2018).
45. Kalinin, K. P. & Berloff, N. G. Polaritonic network as a paradigm for dynamics of coupled oscillators. *Phys. Rev. B* **100**, 245306 (2019).
46. Lerario, G. et al. Room-temperature superfluidity in a polariton condensate. *Nat. Phys.* **13**, 837–841 (2017).
47. Luo, S. et al. Classical spin chains mimicked by room-temperature polariton condensates. *Phys. Rev. Appl.* **13**, 44052 (2020).
48. Whittaker, C. E. et al. Exciton polaritons in a two-dimensional Lieb lattice with spin-orbit coupling. *Phys. Rev. Lett.* **120**, 097401 (2018).
49. Liu, W. et al. Generation of helical topological exciton-polaritons. *Science* **370**, 600–604 (2020).

Methods

Fabrication of optical cavity and nanocavity. For the fabrication of the DBR wafer, six inch quartz wafers were cleaned by soaking in heated 120 °C piranha baths for 10 min followed by a four-cycle deionized water wash. The cleaned wafers were loaded into a vacuum chamber for SiO_2/Ta_2O_5 deposition by electron beam evaporation with an advanced plasma source. Nine pairs of the SiO_2/Ta_2O_5 DBR mirror were deposited at 300 °C. The elevated temperature and high-kinetic-energy plasma bombardments produced sharp interfaces and improved each layer's film density, flatness and surface roughness and hence enhanced the optical quality of the DBR mirrors.

For the thermal compression of the wafer–wafer bonding of the DBR wafer with the patterned gold pillar, the DBR wafers were cleaned with piranha solution (same conditions as the cleaning of the quartz wafer, mentioned above). A 2D array of squared gold pads (side length, 250 μm; thickness as designed; separation, 750 μm) were deposited on the surface of the DBR wafers by electron beam evaporation. Two of the same gold-patterned wafers were cleaned by deionized water for four cycles before being loaded into the wafer bonder. The wafers were aligned according to the position of the gold pads followed by slowly increasing the compressive force to 20,000 N. The chamber was slowly ramped up to 300 °C in 30 min and kept there for 100 min before naturally cooling overnight with the compressive force on. The bonded wafer was finally diced into small chips for crystal growth. One can also use copper or SiO_2 as the bonding spacer at the expense of a higher processing temperature.

Synthesis of halide perovskites. All of the chemicals were purchased from Sigma-Aldrich Chemical and used as received. Unless specified, all the solution preparation and crystal growth were carried out in an argon-filled glove box (though there was no noticeable quality difference compared with ambient condition synthesis).

For the growth of the all-inorganic halide perovskite ($CsPbBr_3$) thin crystals in the nanocavity, we used an inverse temperature crystallization. First, 1 ml dimethyl sulfoxide DMSO was added into a caesium bromide (CsBr, 1 mmol, 0.212 g) and lead bromide ($PbBr_2$, 2 mmol, 0.734 g) powder mixture in a 10 ml vial. Violent vibration was used until all powder dissolved at room temperature before filtration to remove possible impurities. A drop of the prepared solution was dropped at the edge of the fabricated DBR nanocavity, and 10 min was given until the cavity space was fully filled by the solution through capillary force. The DBR nanocavity with $CsPbBr_3$ precursor solution was put on a hot plate, and the temperature was ramped up to 120 °C in 2 min and kept there for 24 hours. The perovskite growth locations were random in the cavity. After the crystal growth, the DBR nanocavity with crystals was put in a vacuum chamber to remove possible residual solvent.

For the growth of 2D halide perovskite (PEPI) thin crystals in the nanocavity, the method is an induced peripheral crystallization. First, 1 ml γ-butyrolactone was added into a phenylethylamine iodide (1 mmol, 0.249 g) and lead iodide (2 mmol, 0.922 g) powder mixture in a 10 ml vial. Violent vibration was used until all the powders were dissolved at room temperature before filtration to remove possible impurities. A drop of the prepared solution was dropped at the edge of the fabricated DBR nanocavity, and 10 min was given until the cavity space was fully filled with the solution through capillary force. The DBR nanocavity with PEPI precursor solution was put on a hot plate, the temperature was ramped up to 100 °C in 2 min and kept there overnight. The temperature was slowly cooled at a rate of 10 °C h^{-1} to room temperature to let the PEPI crystal grow. The perovskite growth locations were random in the cavity.

For the growth of the hybrid halide perovskite (methylammonium lead chloride) thin crystals in the nanocavity, we adopted an inversion temperature precision gradient crystallization. First, 1 ml mixed solvent (*N*,*N*-dimethylformamide and dimethyl sulfoxide, 1:1, v/v) was added into a methylammonium chloride (1 mmol, 0.067 g) and lead chloride (1 mmol, 0.278 g) powder mixture in a 10 ml vial. Violent vibration was used until all the powder was dissolved at room temperature before filtration to remove possible impurities. A drop of the prepared solution was dropped at the edge of the fabricated DBR nanocavity, and 10 min was given until the cavity space was fully filled with the solution through capillary force. The DBR nanocavity with methylammonium chloride precursor solution was put on a hot plate, and the temperature was ramped up to 80 °C in 2 min and maintained there for 4 h before ramping up to 100 °C and being kept there for 24 h. The perovskite growth locations were random in the cavity. After the crystal growth, the DBR nanocavity with crystals was put in a vacuum chamber to remove possible residual solvent.

For the CVD growth of all-inorganic $CsPbBr_3$ perovskite, the all-inorganic perovskites shown in the Supplementary Information were synthesized via a one-step approach using a single-zone CVD system. Freshly cleaved high-quality mica substrates (1.2 cm × 4 cm) were placed on top of a quartz crucible containing a powder mixture of CsBr (20 mg) and $PbBr_2$ (30 mg) before being sent into the centre of a CVD tube. The tube was pumped down and fed with Ar (99.999% purity) four times. Tube pressure was maintained at ambient pressure with an Ar flow rate of 30 sccm. The system was first heated to 400 °C within 24 min, followed by heating from 400 °C to 500 °C within 4 min and being maintained for 20 min. After the growth of crystals, the tube was cooled to room temperature naturally.

Characterizations of halide perovskites. For the AFM, the nanocavities were opened by brute force with tweezers to expose the perovskite crystals before AFM measurements. The AFM images and height profiles of crystals were taken with a Park Systems NX10 AFM instrument in tapping mode and analysed with XEI software. Only the standard plane flattening process was used in our AFM data processing, this is a basic plane levelling used to remove the sample tilting effect from the image acquisition process.

All optical microscopy images of the halide perovskite crystals were taken using an Olympus microscope. Fluorescence microscopy images of PEPI and $CsPbBr_3$ were taken using the same Olympus microscope. The fluorescence microscopy image of $MAPbCl_3$ was taken by a Zeiss confocal microscope under ultraviolet excitation.

X-ray diffraction pattern measurements were taken using a D8 Discover GADDS powder X-ray diffractometer with Cu Kα (wavelength, $\lambda = 1.54056$ Å).

For the ultraviolet–visible absorption spectrum and steady-state PL measurements, all absorption spectrum measurements were taken using a home-built ultraviolet–visible transmission set-up, which utilizes a collimated white lamp source and an Andor spectrometer equipped with a 2D electron multiplying charge coupled device. The PL spectra were performed by the same system. A 250 fs optical parametric amplifier pulse laser with a repetition rate of 20 kHz was used to pump non-resonantly.

All scanning electron microscopy images were taken with a FEI Nova NanoSEM 650.

The PL lifetime was measured using a home-built multifunctional microscope integrated with a time-correlated single-photon counting system. A femtosecond pulsed laser centred at 808 nm (Coherent Mira 900-F) was used for second harmonic generation at 404 nm via a barium borate crystal, and the produced 404 nm laser was fibre coupled to the microscope and focused on the samples through an objective lens. The PL was collected by the same objective and fibre coupled to a single-photon counting module (Excelitas SPCM AQRH 13) after blocking the 404 nm excitation. The PL photon counts were then time correlated (IDQuantique ID 900) with the sync signal from the pulsed laser to build the histogram of photon arrival time, from which PL lifetime can be extracted. Nanocavities were opened by brute force with tweezers before lifetime measurements.

Optical measurements of polariton. The optical measurements were performed using a home-built transmission set-up at room temperature as shown in Supplementary Fig. 15. A 250 fs optical parametric amplifier pulse laser with a repetition rate of 20 kHz was used to achieve non-resonant excitation (470 nm centre wavelength). A Meadowlark Optics reflective liquid-crystal phase-only spatial light modulator was used to generate excitation laser patterns. The hologram was computed with a Gerchberg Saxton algorithm and transferred to an objective (Nikon ×40 Plan Fluor ELWD, numerical aperture = 0.6) with a Fourier imaging configuration to generate a desired laser pattern on the focal plane. The PL was collected in a transmission configuration. The diameter of each focused laser spot was around 1.5 μm. From the other side of the microcavity, another objective was used to collect the PL. The k-space images can be obtained by a Fourier imaging configuration with two achromatic tube lenses. An Andor spectrometer equipped with a 2D electron multiplying charge coupled device was used to measure the energy-resolved polariton dispersions. A charge coupled device camera was used to obtain 2D k-space images and real-space images by flipping the first achromatic tube lens. A long-pass filter was used to filter the excitation laser.

The linear-polarized PL dispersions can be measured with a halfwave plate and a linear polarizer (as shown in Supplementary Fig. 15). A rotation stage was used to rotate the sample to obtain the dispersions along the *x* and *y* axes in Fig. 1g. The cross-section of the two polariton branches in k-space at the diabolic points in Fig. 1h was measured with two narrow-band Semrock bandwidth filters.

Reporting summary. Further information on research design is available in the Nature Research Reporting Summary linked to this article.

Data availability

The authors declare that the main data supporting the findings of this study are available within the paper. Extra data are available from the corresponding authors upon reasonable request. Source data are provided with this paper.

Acknowledgements

We thank P. James Schuck and F. Xue for reading the manuscript and valuable comments and A. Gao from SVOTEK Inc. for assisting with the high-quality DBR mirror coating. W.B. and K.P. acknowledge support from the Office of Naval Research (award no. N00014-21-1-2099) and National Science Foundation (award no. OIA-2044049). W.B. thanks the CAREER support from the National Science Foundation (award no. DMR-2143041). X.Z. and R.T. thank the support by the Gordon and Betty Moore Foundation (award no. 5722) and the Ernest S. Kuh Endowed Chair Professorship. S.K.-C. and L.H. acknowledge funding from the Canada Research Chairs programme and the Army Research Office (W911NF1810149). The work of Q.L. and G.R.F. was supported by the US Department of Energy, Office of Science, Basic Energy Science, Chemical

Sciences, Geosciences, and Biosciences Division. Use of the Center for Nanoscale Materials, a US Department of Energy Office of Science User Facility, was supported by the US Department of Energy, Office of Basic Energy Sciences under contract no. DE-AC02-06CH11357.

Author contributions

W.B., X.Z., R.T. and K.P. initiated the project and conceived the experiments. R.T. fabricated the microcavities and grew and characterized the perovskite materials. K.P. performed all optical measurements except lifetime characterizations. Q.L. and G.R.F. performed the PL lifetime experiments. S.K.-C., D.J. and L.H. provided valuable insight and suggestions. W.B. and X.Z. supervised the whole project. R.T., K.P. and W.B. prepared the initial draught of the manuscript. K.P., W.B., R.T. and X.Z. led the efforts in revising the manuscript with the other authors' participation.

Competing interests

The authors declare no competing interests.

Additional information

Supplementary information The online version contains supplementary material available at https://doi.org/10.1038/s41563-022-01276-4.

Correspondence and requests for materials should be addressed to Xiang Zhang or Wei Bao.

Peer review information *Nature Materials* thanks Natalia Berloff, Hui Deng and the other, anonymous, reviewer(s) for their contribution to the peer review of this work.

Reprints and permissions information is available at www.nature.com/reprints.